THE ASTRONOMICAL JOURNAL, 124:3313–3324, 2002 December

HUBBLE SPACE TELESCOPE OBSERVATIONS OF THE WINDBLOWN NEBULA NGC 7635[1]

BRIAN D. MOORE
Department of Physics and Astronomy, Rice University, Houston, TX 77005-1892

DONALD K. WALTER
Department of Physical Sciences, South Carolina State University, Orangeburg, SC 29117-7296

J. JEFF HESTER AND PAUL A. SCOWEN
Department of Physics and Astronomy, Arizona State University, Tempe, AZ 85287-1504

AND

REGINALD J. DUFOUR AND BRENT A. BUCKALEW
Department of Physics and Astronomy, Rice University, Houston, TX 77005-1892
Received 2002 March 10; accepted 2002 September 4

ABSTRACT

We present *Hubble Space Telescope* observations of the northern part of NGC 7635, a circular shell around the O6.5 IIIf star BD +60°2522. The nebula, which lies within the large emission-line region S162, is notable not only for its symmetric shell, but also for a complex of "cometary" knots close to the central star. Our observations include spectra taken with the Space Telescope Imaging Spectrograph and narrowband images taken with the Wide Field Planetary Camera 2. The high spatial resolution of these data reveals the knots to be the ionized edges of a much larger mass of neutral material, with strong photoevaporative flows toward the central star. The cometary appearance of the knots is produced by the intersection of two ridges, one in the plane of the sky and the other 65° relative to it. Stratification in the emission from the shell can also be seen, the result of shock heating as material is swept into the expanding shell. We also see for the first time a small loop of emission between the central star and the cometary knot complex. We propose that this was formed by the collision between the strong stellar wind and the photoevaporative flow from the closest and brightest of these knots.

Key words: H II regions — ISM: individual (NGC 7635) — ISM: kinematics and dynamics — stars: individual (BD +60°2522) — stars: mass loss

1. INTRODUCTION

1.1. *Background*

The ionized shell nebula NGC 7635 is part of the larger emission complex S162, located in the Perseus arm of the Galaxy. The remarkable spherical symmetry of the nebula has earned it the nickname "Bubble Nebula." NGC 7635 includes a number of features of interest, the most obvious being the bubble itself. Especially notable is the large offset between the "central" star BD +60°2522 and the geometric center of the bubble, about two-thirds of its diameter. An arcade of bright emission knots appears within the bubble's perimeter a short distance west of the central star. Based on their appearance, these inner knots are often referred to in the literature as "cometary" (Johnson 1974). The bubble is nested within an ionized cavity with clusters of bright knots along the outer perimeter, the nearest and brightest of which lie to the north of the star. The overall morphology of the region suggests that BD +60°2522 is its primary, if not sole, source of ionization. Conti & Alschuler (1971) classified the star ($V = 8.7$ mag) as an O6.5 IIIf; its mass-loss rate is $10^{-5.76}\ M_\odot\ \mathrm{yr}^{-1}$ (Leitherer 1988).

NGC 7635 has attracted the attention of a number of investigators over the past 25 years. The radio study by Israel, Habing, & de Jong (1973) established it as a blister H II region on the edge of the same molecular cloud that includes S162. Barlow, Cohen, & Gull (1976) found that the reddening in the nebula followed the normal Whitford (1958) law, with point-by-point variations in the total extinction A_V spanning 2–4 mag. Temperatures, densities, and chemical abundances within the nebula have been the focus of spectrophotometric studies (e.g., Sabbadin & Bianchini 1977; Talent & Dufour 1979). Thronson et al. (1982) mapped the nebula in the infrared and radio regimes. Lynds & O'Neil (1983) used long-slit spectra and photographic images taken through narrowband interference filters to study the kinematics and ionization structure of the bubble and nearby knots. More recently, Christopoulou et al. (1995) used long-slit echelle spectra to derive a kinematic model of the nebula. Their article is a good starting point for examining past work on NGC 7635, as they summarize numerous studies from the literature.

The consensus from the literature is that the bubble is the result of the ram pressure of the central star's wind sweeping up ambient material into a thin shell. The value of $F([\mathrm{O\ III}])/F(\mathrm{H}\beta)$ for the bulk of the nebula is approximately 0.5; by contrast, values as high as 7 are seen in the emission from the shell (Dufour 1989). Coupled with an observed expansion speed of up to 25 km s^{-1} along the line of sight, this suggests the presence of shock-excited material within the bubble. Estimates for the total mass of the shell range from 4.5 $M_\odot$ (Doroshenko 1972) to 12 $M_\odot$ (Icke 1973).

1.2. *Distance to NGC 7635*

An accurate distance to the Bubble Nebula is necessary for a proper interpretation of the morphology and dynamics

[1] Based on observations made with the NASA/ESA *Hubble Space Telescope*, obtained at the Space Telescope Science Institute (STScI), which is operated by the Association of Universities for Research in Astronomy (AURA), Inc., under NASA contract NAS 5-26555.

TABLE 1
NEW OBSERVATIONS OF NGC 7635

Feature	Telescope	Instrument	R.A. (J2000)	Decl. (J2000)	Slit Size (arcsec)	Slit P.A. (deg)
Bubble	*HST*	WFPC2	23 20 42.0	61 12 32	...	...
Inner knots	*HST*	STIS	23 20 42.6	61 11 28	0.2 × 52	114
	Steward 90 inch	Spectrograph	23 20 42.6	61 11 28	2.5 × 240	109
		CCD camera	23 20 37.0	61 12 51	...	...
Rim.....	*HST*	STIS	23 20 48.3	61 12 08	0.2 × 52	52
	Whipple 60 inch	Spectrograph	23 20 48.3	61 12 08	3.0 × 180	90

NOTE.—Units of right ascension are hours, minutes, and seconds, and units of declination are degrees, arcminutes, and arcseconds.

of this system. Values in the literature can be grouped into two ranges: 2.2–2.6 and 3.5–3.6 kpc. Christopoulou et al. (1995) note that the higher range comes from Georgelin (1975), Israel et al. (1973), and Johnson (1982). The Georgelin value was published in a thesis that was not available for review. Israel et al. based their value on two methods. The first was to fit H I 21 cm data to the Galactic rotation model of Schmidt (1965) to produce a distance of 2.4–4.6 kpc. The second method employed the published spectroscopic parallax of BD +60°2522, for a value of 3.6 kpc. We are unable to reproduce that value from the data cited in their article, instead deriving a value of 2.5 kpc. Johnson (1982) references a value of 3.6 kpc from Johnson (1980), again based on the spectroscopic parallax of BD +60°2522. The value used for the expected absolute magnitude of the star (−6.3) is significantly higher than that assumed by others (−5.5) for its stellar type. This approach is inherently risky given the large scatter in M_V for a given spectral type for O stars (see, e.g., Conti et al. 1983).

We favor those sources within the lower of the two ranges. Humphreys (1978) calculated a distance of 2.6 kpc from the spectroscopic parallaxes of 16 stars in the Cas OB2 association, of which BD +60°2522 is also considered a member; she did not, however, include it or two other stars lacking clearly defined stellar types. Garmany & Stencel (1992) went even further, recomputing the distances to 24 associations employing the cluster-fitting method on data in the literature. Unlike previous authors, they standardized the distance calculations by fitting the associations to the same zero-age main sequence (ZAMS); they omitted O-type stars in the ZAMS fitting, bypassing the M_V calibration problem discussed above. Their distance to the Cas OB2 association is 2.2 kpc. Given the statistically larger samples in these studies and their avoidance of the O star problem, we adopt the mean of the two results (2.4 kpc) as the distance to NGC 7635.

1.3. *This Study*

An understanding of NGC 7635 is important to the understanding of the mass-loss history of young, high-mass stars, which are precursors to supernovae. It is also useful for developing a better understanding of the effect of wind-driven shocks in the interstellar medium. NGC 7635 also contains several high-density knots in close proximity (20″) to an intense stellar wind and radiation field from the central star. The dynamics and evolution of such a system may differ substantially from those of M16 and other relatively quiescent star-forming H II regions.

In this paper, we present data taken with the Wide Field Planetary Camera 2 (WFPC2) and Space Telescope Imaging Spectrograph (STIS) aboard the *Hubble Space Telescope* (*HST*). The high spatial resolution of *HST* reveals features previously unseen and offers insight into the geometry and dynamics of the system. We also include data we have taken with several ground-based observatories. An overview of our suite of observations appears in Table 1. Section 2 presents the analysis of our new ground-based and STIS spectra. The imagery is presented and discussed in § 3. A more detailed discussion of the bubble is given in § 4, and that of a previously unseen emission loop in § 5. A summary of our findings is presented in § 6.

2. SPECTRA

2.1. *Observations*

STIS CCD observations of the inner knots and rim of NGC 7635 were made on 1997 October 1–2 and November 25, respectively. In addition, ground-based spectra were obtained in 1998 September at the Steward Observatory 90 inch (2.3 m) telescope and the 60 inch (1.5 m) of Whipple Observatory. The details of all the spectra discussed in this paper are given in Table 2. Calibration of the raw STIS spectra was performed with the IRAF/STSDAS package CALSTIS using calibration files (e.g., flats) more appropriate to the time frame of the actual observations. Ultraviolet spectra of the knots were also attempted with the STIS multianode microchannel arrays, but the high degree of extinction precluded the observation of measurable continuum or line flux.

At each position, STIS was used with a 0.″2 × 52″ slit centered on the feature of interest. The slit length was sufficient to sample the flux from the features as well as that of the local background, providing for its isolation and subtraction. The emission-line fluxes were calculated over a 20″ portion of the slit containing the entire knot. The slit of the Steward spectrograph was centered on the coordinates of the center of the STIS knot's slit. Likewise, the center of the Whipple slit intersected the bubble rim at the same location as our STIS rim position, albeit at a considerably different position angle. The observed and dereddened fluxes for the knots and rim are presented in Tables 3 and 4, respectively.

2.2. *Diagnostic Results*

The diagnostic results from our *HST* and ground-based spectra are summarized in Table 5. Extinction was

TABLE 2
DETAILS OF SPECTROSCOPIC OBSERVATIONS OF NGC 7635

Feature	Instrument/Grating	λ Range (Å)	Exp. Time (s)	Date Taken
Inner knots	STIS/G750M	6480–7050	2160	1997 Oct 1
	STIS/G750M	5450–6020	5620	1997 Oct 2
	STIS/G430L	2904–5714	2740	1997 Oct 2
Bubble rim	Steward/600 line mm^{-1}	4700–7000	640	1998 Sep 17
	STIS/G750M	6480–7050	2700	1997 Nov 25
	STIS/G430L	2904–5714	2300	1997 Nov 25
	Whipple/1200 line mm^{-1}	4230–5230	6000	1998 Sep 27

corrected with the reddening law of Seaton (1979), and temperatures and densities were determined from diagnostic ratios with the STSDAS package NEBULAR, as described by Shaw & Dufour (1995). Our Whipple spectrum has provided the first [O III] temperature for the rim of the bubble, while our Steward spectra allowed us to resolve the spatial variation in density calculated from the [S II] lines, with the minimum and maximum values shown in the table and discussed below. While one must use caution in comparing results for varying slit locations and resolutions, our results compare favorably with those in previous studies, such as that of Talent & Dufour (1979).

Since the STIS spectra were integrated along the spatial direction, only a single value is listed for each ion in Table 5. Note that the extracted area of the STIS slit is approximately equal to that of a single pixel in the Steward spectra (4.0 vs. 4.6 $arcsec^2$). For the Steward spectra, the chlorine density was calculated with the sum of 3 pixels in the spatial direction at the center of the slit; the sulfur lines were sufficiently bright to permit a density calculation at each pixel along the slit.

For a given spectrum, the sulfur and chlorine densities for the knots yield considerably different density values; this is expected, as their emission arises from different parts of the photoevaporative flow toward the star. For the STIS spectra, the large uncertainty in the [Cl III] density is largely due to uncertainty in the flux; the uncertainty in [S II] is largely due to the relative insensitivity of the diagnostic at such high densities.

Figure 1 shows the spatial variation of [S II] density for the Steward spectrum of the inner knots. Distances are given relative to the center of the slit, with the offsets increasing to the northwest (i.e., away from the star). Note the very pronounced rise and fall in density around the peak. Further up the ridge, one sees local fluctuations superposed on a density of a few hundred per cubic centimeter. For both the STIS and Steward long-slit spectra, the foreground contribution was assessed by averaging the flux in a number of pixels toward the center of the bubble. In some instances the foreground subtraction produced negative values; where this occurs the data are ignored, indicated in the plot by arrows pointing to zero density.

TABLE 3
OBSERVED AND EXTINCTION-CORRECTED LINE FLUXES: KNOTS

	STEWARD		STIS	
LINE	$F(\lambda)$[a]	$I(\lambda)$[b]	$F(\lambda)$	$I(\lambda)$[c]
[S II] λ6731	54.3 ± 3.9	21.4 ± 2.5	51.0 ± 2.3	18.9 ± 0.9
[S II] λ6717	32.0 ± 1.9	12.7 ± 1.4	25.8 ± 1.2	9.61 ± 0.47
He I λ6678.....	6.53 ± 0.81	2.63 ± 0.41	7.24 ± 0.58	2.73 ± 0.22
[N II] λ6584	251 ± 8	105 ± 10	272 ± 11.7	107 ± 4.8
Hα (6563 Å).....	688 ± 8	288 ± 27	730 ± 31.3	288 ± 12.9
[N II] λ6548	82.9 ± 3.9	34.9 ± 3.7	84.2 ± 3.7	33.4 ± 1.5
[S III] λ6312	3.88 ± 0.10	1.79 ± 0.18	...	...
He I λ5876.....	16.3 ± 1.1	9.11 ± 1.17	21.3 ± 1.0	11.4 ± 0.5
[N II] λ5755	2.07 ± 0.11	1.24 ± 0.15	2.21 ± 0.22	1.28 ± 0.13
[Cl III] λ5538.....	0.76 ± 0.07	0.52 ± 0.08	0.71 ± 0.22	0.47 ± 0.15
[Cl III] λ5518.....	0.60 ± 0.05	0.41 ± 0.06	0.80 ± 0.35	0.54 ± 0.23
[O III] λ5007.....	76.5 ± 2.4	69.8 ± 9.5	57.6 ± 2.5	52.2 ± 2.3
[O III] λ4959.....	25.1 ± 1.4	23.6 ± 3.5	18.9 ± 0.9	17.7 ± 0.8
Hβ (4861 Å).....	100 ± 4	100 ± 14	100 ± 4.3	100 ± 4.3
He I λ4471.....	...	...	7.08 ± 0.34	9.31 ± 0.45
Hγ (4340 Å).....	...	...	33.9 ± 1.5	49.1 ± 2.2
He I λ4026.....	...	...	1.54 ± 0.40	2.66 ± 0.68
[O II] λ3727.....	...	...	85.3 ± 3.7	178 ± 7.9

[a] Given relative to $F(H\beta) = 100$; similarly for $I(\lambda)$.
[b] $C(H\beta) = 1.17$, using $F(H\alpha)/F(H\beta) = 2.88$.
[c] $C(H\beta) = 1.25$, using $F(H\alpha)/F(H\beta) = 2.88$.

TABLE 4
OBSERVED AND EXTINCTION-CORRECTED LINE FLUXES: RIM

	WHIPPLE		STIS	
LINE	$F(\lambda)$[a]	$I(\lambda)$[b]	$F(\lambda)$	$I(\lambda)$[c]
[S II] λ6731	...	...	26.1 ± 6.1	8.15 ± 1.87
[S II] λ6717	...	...	21.2 ± 4.2	6.65 ± 1.28
He I λ6678.....	...	...	12.7 ± 4.1	4.05 ± 1.28
[N II] λ6584	...	...	82.5 ± 7.9	27.4 ± 2.3
Hα (6563 Å).....	...	...	858 ± 5.6	288 ± 12.6
[N II] λ6548	...	...	25.4 ± 7.0	8.58 ± 2.3
He I λ5047.....	0.31 ± 0.05	0.30 ± 0.05	...	...
He I λ5016.....	3.07 ± 0.06	3.00 ± 0.06	...	...
[O III] λ5007.....	283 ± 0.8	277 ± 0.5	245 ± 16.7	219 ± 8.2
[O III] λ4959.....	86.5 ± 0.3	85.2 ± 0.2	90.3 ± 7.6	83.4 ± 5.2
He I λ4922.....	1.33 ± 0.05	1.32 ± 0.05	...	...
Hβ (4861 Å).....	100 ± 4	100 ± 3	100 ± 8.0	100 ± 5.7
O II λ4641.....	0.18 ± 0.05	0.19 ± 0.05	...	...
He I λ4471.....	4.32 ± 0.10	4.61 ± 0.10	...	...
He I λ4388.....	0.41 ± 0.06	0.44 ± 0.06	...	...
[O III] λ4363.....	0.78 ± 0.09	0.85 ± 0.10	...	...
Hγ (4340 Å)	43.6 ± 0.3	47.6 ± 0.3	20.8 ± 3.0	32.2 ± 4.3
C II λ4267.....	0.176 ± 0.06	0.182 ± 0.07	...	...
[O II] λ3727.....	...	...	45.4 ± 10.6	107.7 ± 24.4

[a] Given relative to $F(\mathrm{H}\beta) = 100$; similarly for $I(\lambda)$.
[b] $C(\mathrm{H}\beta) = 0.242$, from $I(\mathrm{H}\gamma)/I(\mathrm{H}\beta) = 0.476$.
[c] $C(\mathrm{H}\beta) = 1.46$, from $I(\mathrm{H}\alpha)/I(\mathrm{H}\beta) = 2.88$.

TABLE 5
NEW T_e AND N_e RESULTS FOR NGC 7635

Feature	Source	T_e([N II]) (K)	T_e([O III]) (K)	n_e([S II]) (cm^{-3})	n_e([Cl III]) (cm^{-3})
Rim.....	STIS	...	...	1230	...
	Whipple	...	8180	...	...
Knots.....	STIS	7950	...	11300^{+16700}_{-4550}	1330^{+9870}_{-1330}
	Steward	8560	...	85–7560	5180

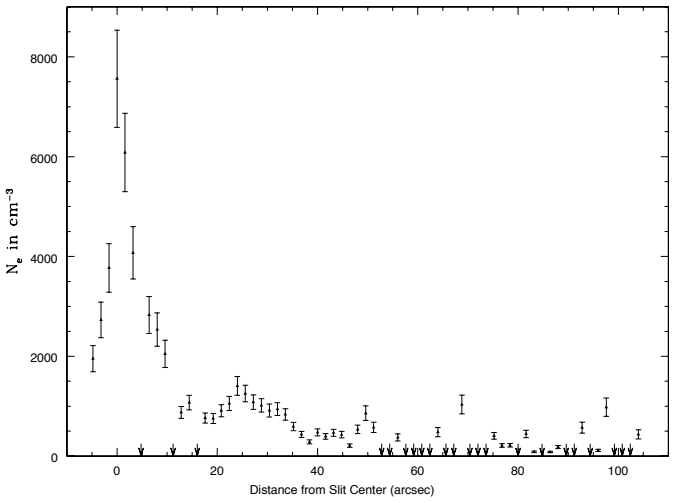

FIG. 1.—Pixel-to-pixel variation along the slit of the [S II] electron density for the Steward spectrum of the inner knots. The peak density corresponds to the brightest of the inner knots, with distance increasing away from the central star. Arrows indicate where background subtraction produces negative flux values.

2.3. *Surface Brightness Profiles*

For sufficiently bright lines, the spatial distribution of flux in the STIS spectra can be preserved and examined. Comparisons of these lines can provide valuable information about the ionization structure within the observed region. The fluxes of three bright lines in our STIS spectra were extracted and normalized to their peak values: [O III] λ5007, [N II] λ6584, and Hα (6563 Å). The results for the knot and rim spectra are shown in Figures 2 and 3, respectively.

The profiles of the knot spectrum are presented in Figure 2, again with positive offsets toward the northwest and negative to the southeast. In this plot the morphology of the photoevaporative flow is evident. The STIS line profiles in the knot spectrum show large-scale variation in emission over short distances, similar to that seen in the Steward spectra. The offset of the [O III] line from that of Hα is real, indicating the ionization structure within the flow. Note that the size of the offset (1″) is at the resolution limit of most ground-based spectra. The ionization structure within the flow is also manifested to a lesser degree in the difference between the [N II] and Hα emission morphology.

As might be expected, the profile of the rim spectrum is of an altogether different character. Scans across the rim are shown in Figure 3, with negative offsets within the bubble

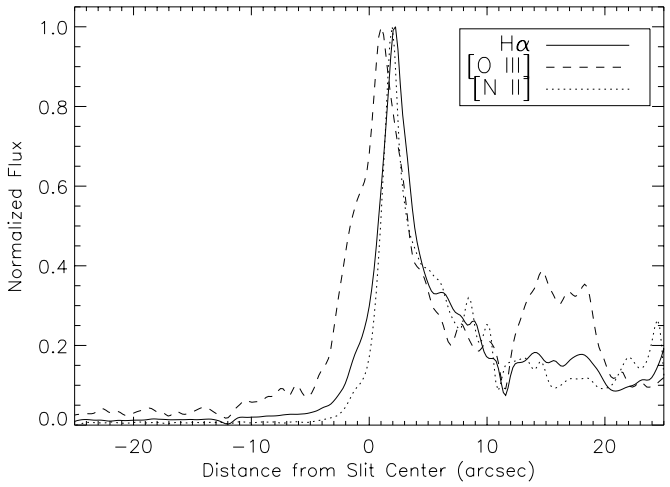

FIG. 2.—Normalized surface brightness spatial scan from the STIS spectra across the inner knots for several emission lines. The central star lies beyond the left edge of the plot. Note the offset of the [O III] emission relative to that of Hα.

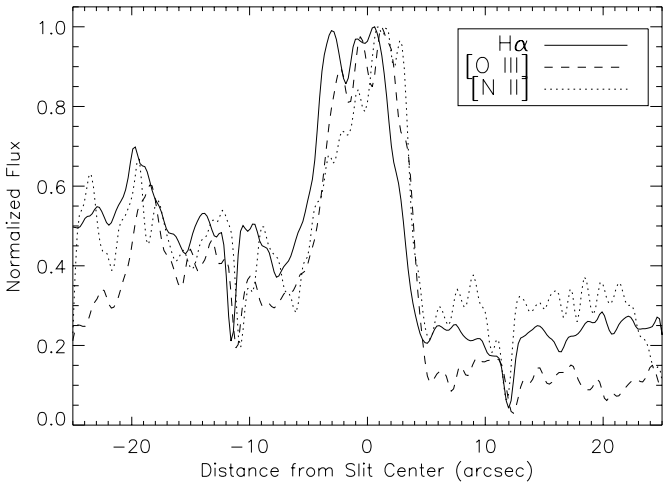

FIG. 3.—Same as Fig. 2, but for the STIS spectra across the rim. Note the offset of both the [N II] and [O III] emission relative to that of Hα.

perimeter and positive offsets beyond it. A three-bump structure in the surface brightness—evident in all three lines but most pronounced in [O III]—is seen as the scan crosses the rim of the bubble. These small-scale fluctuations are the product of the undulating surface of the bubble, visible even in the ground-based images. The bubble morphology will be discussed further in § 3.

In contrast to the knot spectrum, the rim spectrum shows [N II] shifted away from the star relative to Hα and morphologically similar to the [O III] emission. This can be explained by the expansion of the shell, sweeping up and shock heating the material from the H II region. The preshock material is in ionization equilibrium with the star, so the shock itself need not ionize the medium. In fact, the spatial agreement between [O III] and [N II] implies that the shock speed is not high enough to ionize N^+ to N^{++}. The nature of the bubble expansion is discussed in § 4.

2.4. *Abundance Results*

We have inferred ionic abundances from the integrated STIS, Whipple, and Steward spectra using the current STSDAS NEBULAR package (Shaw & Dufour 1995). All transitions were considered to arise purely from electron collision alone, with the following exceptions: The He^+ abundances were derived from the recombination volume emissivities of Smits (1996). The C^{++} abundance was calculated using the optical C II line λ4267; the abundance was derived from this recombination line via the method employed by Esteban et al. (1998). Our results are presented in Table 6, with the results of Talent & Dufour (1979) included for comparison.

There are two values quoted for the O^{++} abundance from the Whipple spectrum of the rim: the first value was derived from the 5007 Å collisional line, and the value in parentheses was derived from the 4641 Å recombination line, derived via the same method as C^{++}. The large difference between the O^{++} abundances derived from recombination and collisional lines can be explained by temperature differences within the rim material—namely, the combination of emission from the photoionized and shock-heated regions in spectra of the rim.

The table also includes the oxygen and nitrogen abundances for our STIS observations, based on the common assumptions $O = O^+ + O^{++}$ and $N^+/N = O^+/O$. For comparison, the results of Talent & Dufour (1979) are included, as well as the values expected from the abundances of Shaver et al. (1983) at the assumed Galactocentric radius (11.7 kpc).

Both the He^+ abundance of the rim (11.16) and of the knots (10.94) exceed the total helium abundance expected from Shaver et al. (10.78). The difference between the rim and knots could be due solely to the differing degree of ionization, or due to enrichment in the rim by the stellar wind from BD $+60^\circ 2522$. The N/H and O/H in the knot, and N/H in the rim, are consistent with Shaver et al.; the O/H of the rim is lower by nearly a factor of 2. We do not con-

TABLE 6
NEW ABUNDANCE RESULTS FOR NGC 7635

Feature/Source	He^+	N^+	O^+	O^{++}	S^+	S^{++}	Cl^{++}	C^{++}	O	N
Knots/STIS	10.94	7.65	8.75	7.66	6.55	...	5.28	...	8.78	7.69
Knots/Steward	10.81	7.52	...	7.65	6.30	6.83	5.04	...	...	...
Rim/STIS	11.16	6.97	8.11	8.24	5.83	...	...	...	8.49	7.34
Rim/Whipple	11.11	...	...	8.31 (8.47)	...	...	...	8.63	...	...
Knots/T&D 1979	10.73	7.50	8.70	7.42	6.61	6.92	4.84	...	8.72	7.52
Rim/T&D 1979	10.91	6.92	8.29	8.07	5.90	6.88	4.97	...	8.49	7.12
Shaver et al. 1983	...	...	...	...	...	...	...	...	8.60	7.42

sider this difference to be real, but rather a result of inaccuracies in the ionic abundances for oxygen due to the aforementioned temperature structure of the rim.

The abundances from the Whipple spectrum are insufficient to infer a total carbon abundance, but we can draw inferences from our total suite of abundances. The low S^+/S in the knots implies the same for the rim, since it is at a higher degree of ionization; thus, we can infer that $C^+/C$is also small from the similarity in ionization potential. Also, Talent & Dufour (1979) show that $Ar^{++}/Ar = 0.6$ in the rim; since the window of ionization potential for Ar^{++} is bracketed by that of C^{++}, then $C^{++}/C \geq 0.6$. Combined with our abundance, this yields $C = 8.63$–8.85. Using the O abundance from the knots, this implies $C/O = -0.14$ to 0.06. Compared with $C/O = -0.25$ for Orion (Esteban et al. 1998), this suggests that carbon is likely enhanced relative to oxygen within the rim. A detailed study of the composition of the stellar wind could resolve whether this enhancement is due directly to the wind material or to some other process (e.g., the destruction of carbon-rich dust by the shock).

3. IMAGERY

3.1. *Observations*

WFPC2 imagery of the northern perimeter of NGC 7635 was obtained on 1999 April 19. Observations were concentrated on the northern part of the spherical shell and the inner knots. Several bright knots belonging to S162 also lie within the field of view. Figure 4 shows a composite of images of NGC 7635 and its surroundings obtained with the Palomar 1.5 m telescope, with the field of view of our WFPC2 images superposed. Additional images were taken with the Steward Observatory 90 inch telescope. Details of all the observations are presented in Table 7.

The characteristics and performance of the WFPC2 camera are described by Trauger et al. (1994). Two 1000 s

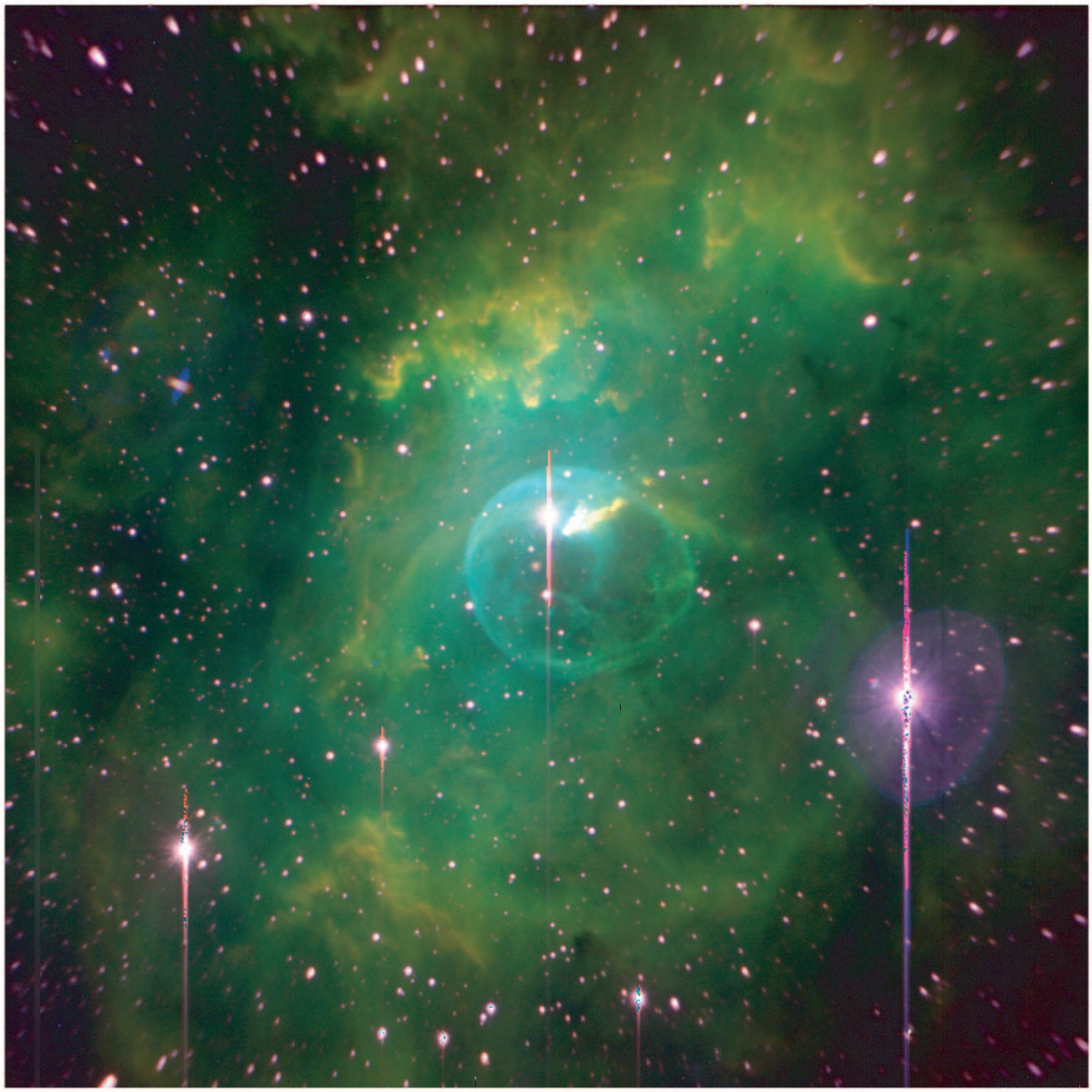

FIG. 4.—Color-coded image of NGC 7635 and its surroundings. This image was taken with the Palomar 1.5 m. Emission from [O III] is shown in blue, emission from Hα in green, and emission from [S II] in red.

TABLE 7
DETAILS OF *HST* WFPC2 AND STEWARD OBSERVATIONS OF NGC 7635

Filter	Exp. Time (s)
WFPC2 (1999 Apr 19):	
F656N	2 × 1000
	2 × 70
F502N	2 × 1000
	2 × 80
F658N	2 × 1000
	2 × 80
F673N	2 × 1000
	2 × 80
F487N	2 × 600
	2 × 80
F547M	2 × 160
	2 × 10
Steward (1998 Sep 28):	
5013 Å/30	4 × 600
6560 Å/29	3 × 600
6728 Å/35	2 × 300

exposures were taken in the following filters centered on emission lines of interest: F502N ([O III] λ5007), F656N (Hα), F658N ([N II] λ6584), and F673N ([S II] $\lambda\lambda$6717, 6731). A series of short exposures was also taken to ensure coverage of regions bright enough to exceed the full-well capacity of the CCDs. To evaluate the degree of reddening, a 2 × 600 s exposure was taken in the F487N (Hβ) filter, with 2 × 2 on-chip binning to increase the signal-to-noise ratio. A 2 × 160 s exposure was taken through the line-free F547M filter to assess the contribution of reflected stellar continuum in the line images.

Each pair of exposures was reduced and combined to remove cosmic rays. The frames were then mosaicked with a routine based on the astrometric solution of Holtzman et al. (1995b) that resamples the images onto a grid with a common linear spatial scale. Visual inspection shows a relative alignment of the final mosaics within 0.2 pixels. Final mosaics of four of the line images are presented in Figure 5. A color-coded composite of three of these is shown in Figure 6. The position angle of the field of view for these data is 4° east of north. One pixel in the mosaics translates to 3.6×10^{15} cm on a side at the assumed distance of 2400 pc.

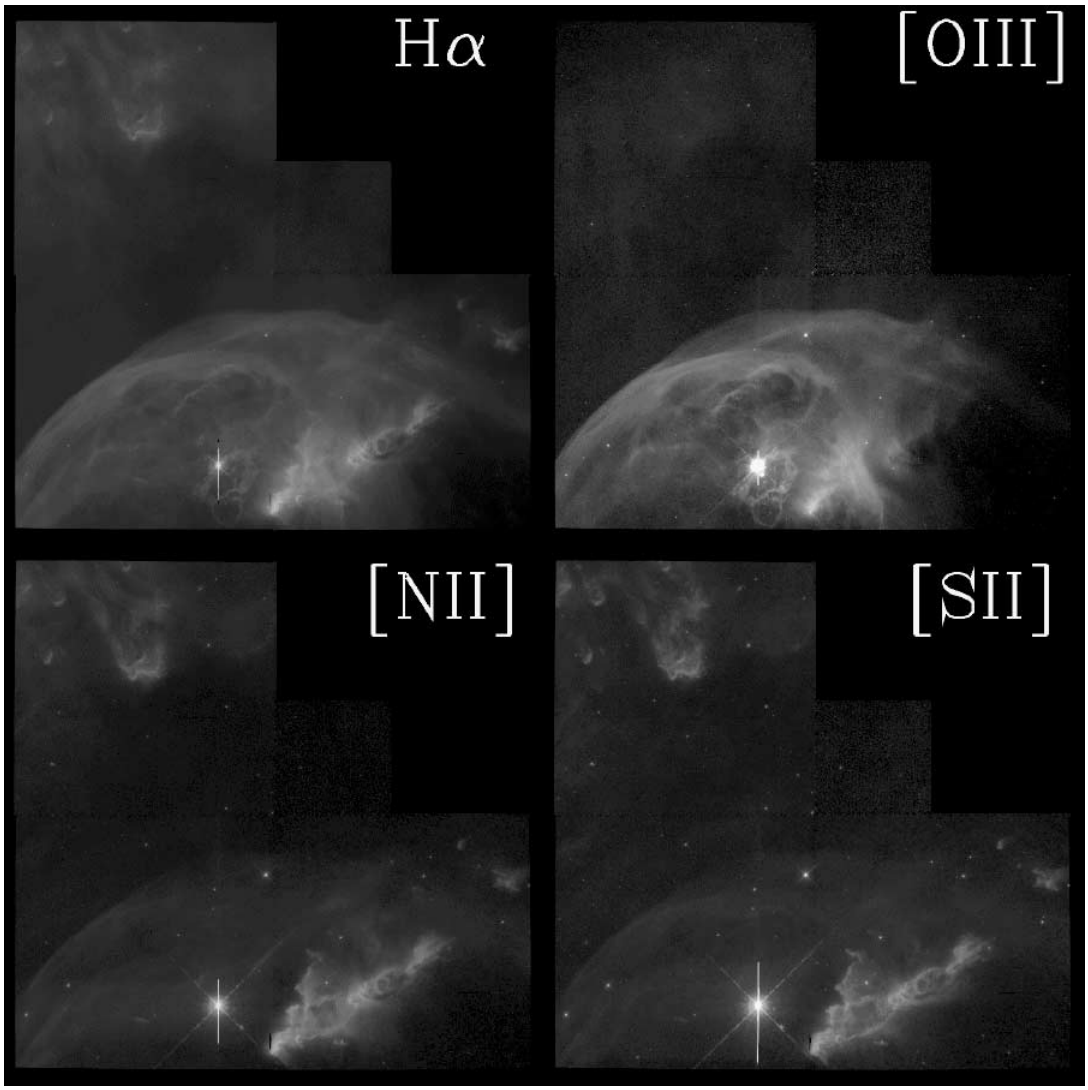

FIG. 5.—Mosaics of individual line images taken with WFPC2. The top images show the nebula in the light of Hα and [O III]; the bottom show those in [N II] and [S II]. The images are displayed with individual logarithmic stretches, to afford comparisons over a large range in surface brightness.

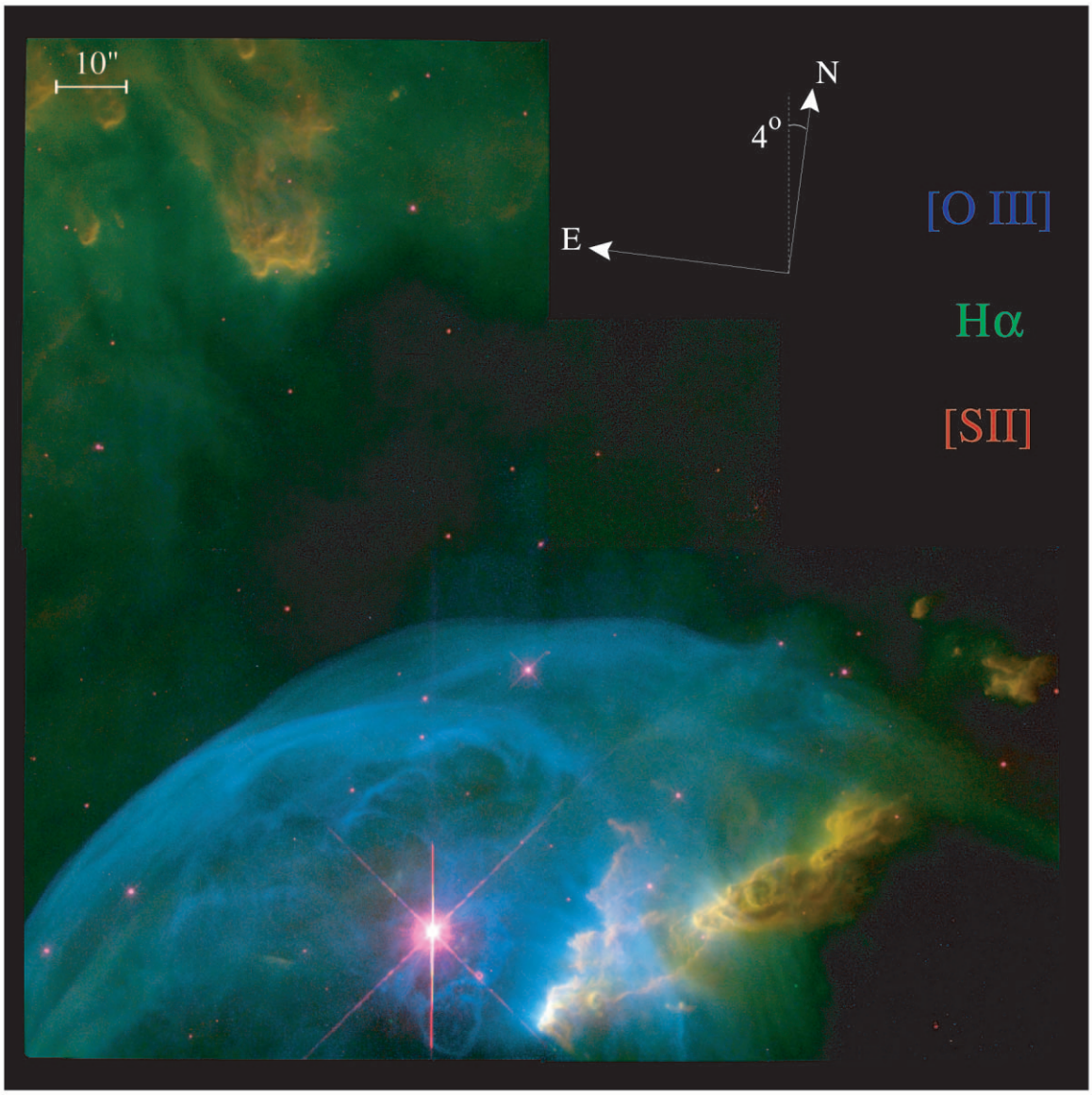

FIG. 6.—Color-coded composite of the WFPC2 images of NGC 7635. Emission from [O III] is shown in blue, emission from Hα in green, and emission from [S II] in red.

Flux calibration of the images followed the prescription of Holtzman et al. (1995a), and the exposures were reduced to isolate the line flux from a single ion as follows: The continuum flux derived from the F547M images was scaled by the widths of the individual filters and subtracted from the individual images. A further correction was needed in order to isolate the Hα and [N II] fluxes for the F656N and F658N exposures. The width of the F656N filter is such that 15% of the [N II] flux is admitted along with the intended Hα flux. Similarly, 5% of the Hα flux is admitted through the F658N filter. To eliminate this, the corresponding fraction of the flux of the calibrated F658N image was subtracted from the F656N, producing an Hα image. This Hα image was in turn scaled appropriately and subtracted from the F658N image.

3.2. *Results*

Our WFPC2 images of the northern portion of the NGC 7635 bubble show a surface characterized by bright arcs and numerous small-scale condensations. As noted before, these features arise from density variations caused by the swept-up material and variation in the line-of-sight emission measure produced by the corrugated surface of the bubble. The relative shift in the peak Hα and [O III] emission from the bubble observed in the spectra manifests itself in the images as a deepening in the bluish tint at its outer edge.

Two complexes of photoionized knots fall within the WFPC2 field of view: the inner "cometary" knots to the west of the central star, and a series of knots to the north. As is apparent from ground-based images, the northern knots have an "elephant trunk" morphology, commonly seen in H II regions. The concentration of Hα emission at their perimeters toward the star implies that they lie close to the plane of the sky, about 1 pc from the star. The striations emanating from the knots toward the star are indicative of photoevaporative flow; attenuation of the O^+-ionizing stellar flux by the flow explains their comparatively low [O III] emission.

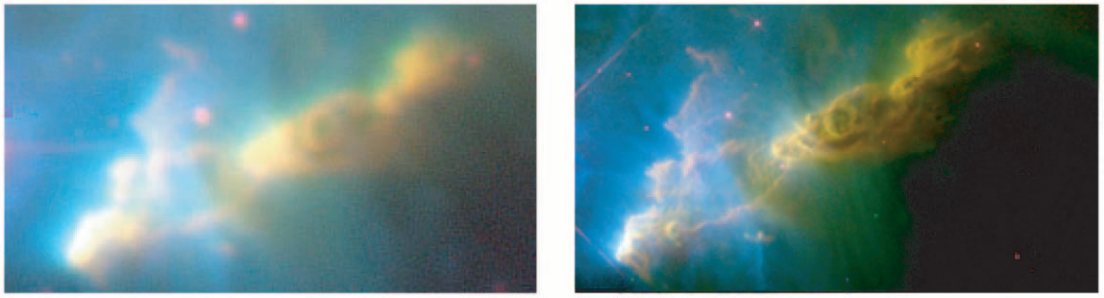

FIG. 7.—Observations of the western knots in NGC 7635. The left image was taken with the Steward 90 inch; the right was taken with WFPC2. The color coding is the same as employed in Fig. 6.

The other complex of knots lies west of the star within the bubble perimeter. In contrast to the northern knots, the nature of these "cometary" knots is revealed in these images, supplanting the confusion in the ground-based imagery. This series of knots is now resolved into an extremely bright central knot close to the star from which extend two ridges or arcades to the west and north. Despite their relative proximity to the central star, the knots appear to be the ionized edges of a much larger region of material. Furthermore, this material shadows the western extent of the bubble material from the ionizing flux of the central star, further evidence of the bubble's dependence on photoionization as its chief emission mechanism. The position of these knots roughly corresponds to the upper edge of a CO cloud seen by Thronson et al. (1982).

As we pointed out in our emission profiles extracted from the spectra, the images of the knots exhibit the morphological hallmarks of photoevaporative flow. Material can be seen streaming upward from the ionized interface toward the star. The brightness of these knots compared with those to the north implies that the inner knots are physically much closer to the star. In fact, there are clear indications of interaction between the bubble and flow from some of the knots. Coherent structures present in the [O III] emission appear to wrap themselves around the various knots in the western ridge. Our images also reveal a complete loop of material lying between the star and the closest of the knots, which we argue in § 5 represents an extreme case of this interaction. We infer from this that these knots are not technically within the bubble and, hence, are not subject to direct exposure to the full effects of the stellar wind or UV flux. The ram pressure of the photoevaporative flow is pushing against the bubble material, preventing the knots from being engulfed by its expansion. A simple physical analog to this would be pushing one's hand against the outside of a balloon; the balloon is distorted around one's fingers, but from the side it appears that they penetrate within.

It is also possible to infer the orientation of the two ridges from the images. The Hα surface brightness of the northern ridge drops radically over a small change in the projected distance from the star. The drop-off in surface brightness for the western ridge is much shallower and takes place over a much larger projected distance. Since the Hα/Hβ ratio is roughly constant in this region, this suggests a radical difference in orientation between them, with the western ridge approximately in the plane of the sky and the northern ridge oriented nearly along the line of sight. From the quantitative analysis of the incident ionizing flux given in Moore et al. (2002, hereafter Paper II), we estimate the orientation for the northern ridge to be $\sim 25^\circ$ relative to the line of sight, or 65° relative to the plane of the sky.

We now have a much improved picture of the overall physical situation in the Bubble Nebula. The namesake bubble is composed of material from within the H II region, swept up by the wind of the central star and photoionized by its UV flux. The knots to the north are pillars of material of the kind commonly seen in ionized nebulae. The "cometary knots" to the west of the star represent the ionized edges of two ridges of dense material oriented in a "flying V" configuration, which forces the advancing bubble to deviate round its surface. To illustrate the unique contribution of *HST* to this physical picture, the Steward and *HST* views of these knots are shown together in Figure 7. The elements of the physical picture are present in the Steward images but can only be appreciated fully with the benefit of hindsight.

4. SPHERICAL SHELL

4.1. *Bubble Expansion*

We can further exploit our *HST* observations of NGC 7635 to examine the nature of the bubble. The expansion of the nebular shell is driven by the ram pressure of the stellar wind, which is balanced by the gas pressure in the shell as well as by the pressure of the external material as it is swept up. The stellar wind material does not interact directly with the bubble; instead, a wind termination shock occurs at a radius determined by the aforementioned pressure balances. If the termination shock occurs at radius R_w, the internal pressure of the bubble is given by

$$P_w/k = \frac{\dot{M}V_\infty}{4\pi R_w^2} = 1.67 \times 10^6 R_w^{-2} \text{ cm}^{-3} \text{ K} \qquad (1)$$

with R_w in parsecs, and using the observed mass-loss rate of $10^{-5.76}\ M_\odot\ \text{yr}^{-1}$ and terminal velocity $V_\infty = 2500$ km s^{-1} (Leitherer 1988). The thermal pressure in the shell can be determined from the spectrum of the rim; with $n_e = 1230$ cm^{-3} and $T_e = 8180$ K, the gas pressure is $P_t/k = 2.2 n_e T_e = 2.2 \times 10^7$ cm^{-3} K. Setting $P_w = P_t$ yields a value for R_w of 0.28 pc, within the bubble as expected.

The expansion speed of the bubble is such that the ram pressure of the swept-up material matches the driving pressure; assuming $n_{\text{He}} = 0.1 n_p$, this is

$$P_w/k = \rho V^2/k \sim 1.4 m_p n_p V^2/k\ , \qquad (2)$$

where V is the speed of the external material in the rest frame of the shock. Note that this includes not only the

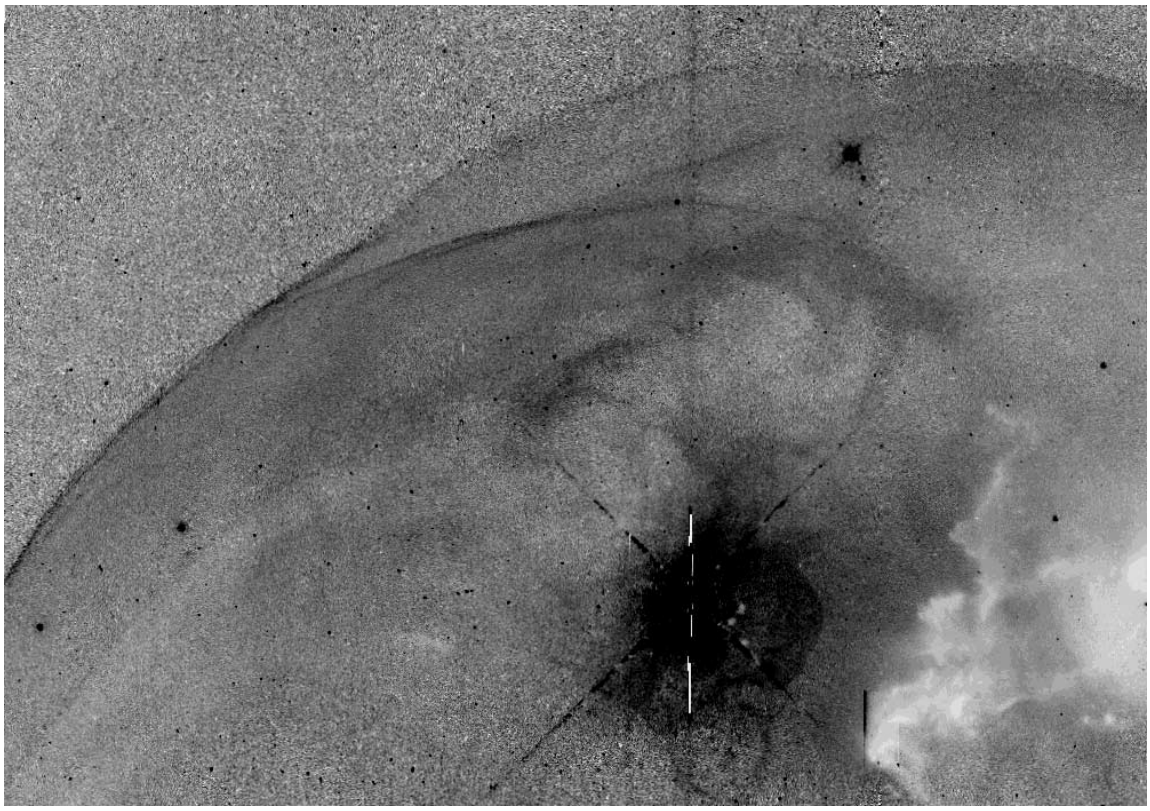

FIG. 8.—Ratio of [O III] to Hα for the WFPC2 field of NGC 7635

bubble expansion, but any bulk flow of the external material. Pressure balance requires a density north of the bubble of $n_p = 280[V/(25 \text{ km s}^{-1})]^{-2} \text{ cm}^{-3}$. The expansion speed of the bubble depends on position about the perimeter; Dufour (1989) measured an equatorial expansion of 25 km s^{-1}, with Christopoulou et al. (1995) observing $\pm$15–20 km s^{-1} relative to the position of the central star (see their Fig. 4).

Because the northward expansion of the bubble occurs in the plane of the sky, it cannot be determined spectroscopically. There is however a noticeable separation of the peak [O III] and Hα emission; this effect can be emphasized by taking the ratio of the two line images (Fig. 8). Since [O III]/Hα at the outer edge is higher than in the bulk of the shell or in the H II region itself, and the shock is not sufficiently fast to raise the ionic abundance of O^{++}, we suggest that this is the result of a nominal amount of shock heating as material is swept up from the surrounding H II region. We can use this hypothesis to derive an estimate for V.

Figure 9 shows a profile in the [O III] and Hα images aligned perpendicular to the bubble surface. In this plot, distance increases away from the shock wave (i.e., distance increases toward the star). The separation of the [O III] and Hα emissions is readily apparent. The initial increase in temperature is related to the Mach number of an adiabatic ($\gamma = 5/3$) shock by

$$\frac{T_2}{T_1} = \frac{(5M^2 - 1)(M^2 + 3)}{16M^2} \tag{3}$$

(Shore 1992, chap. 4, eq. [27]) with $M = V/c_s$, where c_s is the adiabatic sound speed. The initial rise in [O III]/Hα is about a factor of 3; with $T_1 = 8180$ K for the downstream shell material, a trebling of the [O III]/Hα emissivity would require a $T_2 = 11{,}170$ K. With $T_2/T_1 = 1.37$ one derives $M = 1.38$, or $V = 21$ km s^{-1} for $c_s = 15$ km s^{-1}. Thus, equa-

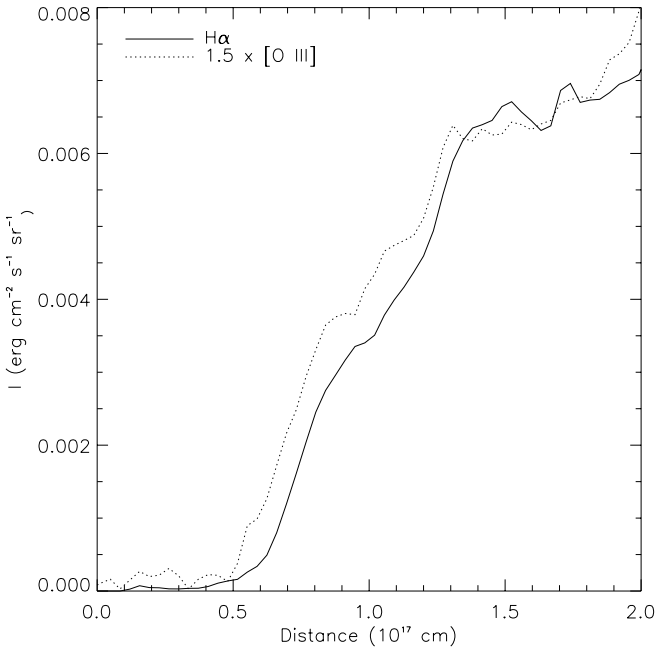

FIG. 9.—Spatial profile of the [O III] and Hα emission from the bubble. The extraction was taken radially at the bubble's nearest point to the star and background-subtracted. The zero point of the x-axis is arbitrary, with distance increasing from the exterior of the bubble to the interior, toward the central star.

tion (2) implies that the density of material toward the north of the bubble is 310 cm^{-3}.

4.2. *Discussion*

Aside from its circularity, one of the more striking features of the bubble in NGC 7635 is the large offset of the central star from the geometric center. One possible explanation is proper motion of the star. Høg et al. (1998) derive a proper motion of 4.5 mas yr^{-1} 40° east of north. Such a proper motion is in the correct direction and would suggest an age for the shell in reasonable agreement with that derived from a constant expansion speed of 25 km^{-1} (14,000 vs. 43,000 yr). These values, however, have a large uncertainty—a factor of 2 in magnitude and 40° in direction.

Another hypothesis presents itself: the observed deviation is tied to the photoevaporative flow from the cavity wall. This can produce a deviation in two ways. The first is the production of a density gradient within the material swept up by the shell. The second is via the ram pressure from the bulk motion of the flow. There is some evidence to support the presence of one or both of these effects. The density external to the northern part of the shell inferred from the shock structure is 310 cm^{-3}. If this were the density throughout the H II region cavity, the stellar UV flux required to ionize it to its observed southern extent (~4 pc) would be $\log Q_0 = 50.4$, much larger than the 49.5 expected for an O6.5 III star (Vacca, Garmany, & Shull 1996).

A density gradient within the surrounding H II region would produce an offset from the central star in the direction of higher density. This holds for NGC 7635, as the proximity of the northern wall would make it the primary contributor of photoevaporated material. Icke (1973) found that an exponential gradient could produce the observed offset, although his densities and timescales for NGC 7635 are probably incorrect.

The ram pressure of material photoevaporated into the H II region could also produce an offset. In this scenario the expansion speed in the rest frame of the bubble is constant along its perimeter. To an observer at rest, the center of the bubble moves away from the star at the flow speed of the swept-up material. The bubble should maintain its circular shape for flow speeds that are small compared with the expansion speed. The offset would again be in the direction toward the dominant contributor, the northern knots.

If the speed of the photoevaporative flow is supersonic, one would expect the collision with the bubble to drive a shock back into the flow. For an isothermal shock, the density is enhanced by a factor of M^2. The flow parameters required are relatively modest. For example, a 16 km s^{-1} flow of density 150 cm^{-3} would produce the 300 cm^{-3} medium encountered by the shell. The postshock flow speed would drop by the same factor, that is, from 16 to 8 km s^{-1}. This is about one-half of the shock speed derived above. This would place the star about one-half of the bubble radius from the geometric center, compared with the value of two-thirds seen in the images. Since these flows would all occur in the plane of the sky, it is not possible to verify this scenario directly. Such a scenario might make an interesting topic for detailed hydrodynamic modeling.

Such a flow could also explain one of the features noted in previous studies from the ground. Christopoulou et al. (1995) claim that the circular bubble lies within a larger "intermediate shell" tangent to the bubble at its northern extreme. We suggest instead that the tangent portion of that shell's perimeter is the bow shock of the flow colliding with the bubble. The emission from the wings of the bow shock would then become confused with the outer ionization edge of the H II region and areas of foreground absorption. While admittedly speculative, we find this explanation for the large-scale morphology of NGC 7635 and S162 ultimately more satisfying than the attempts that have preceded it.

5. EMISSION LOOP

There is an irregular loop of emission seen between the central star and the western knot complex, shown in Figure 8. The loop consists of a bright $10'' \times 18''$ ellipse, with a smaller arc protruding from its southern extreme. While one could construct a number of ad hoc explanations for its existence (e.g., an episode of asymmetric mass loss, a mass ejection offset by subsequent motion of the star), we consider instead that the loop is a consequence of the stellar wind colliding with the observed photoevaporative flow from the knots.

The [O III] and Hα brightness of the loop is roughly uniform about the ellipse, suggesting that points along it are equidistant from the stellar UV flux and, hence, its wind. The ellipse would then be a circular ring 18″ in diameter viewed at an angle of 35° with respect to the plane of the sky. This translates to a ring of radius 3.3×10^{17} cm with its center 3.1×10^{17} cm from the central star, placing the material 4.5×10^{17} cm (0.15 pc) from the central star.

From equation (1), the ram pressure of the stellar wind at a distance of 0.15 pc is $P_w/k = 7.4 \times 10^7$ cm^{-3} K. The photoevaporative material would pile up where its ram pressure matches this value. This condition can be satisfied with reasonable sets of flow parameters; for example, a 400 cm^{-3} flow traveling at 40 km s^{-1}. If the flow is supersonic, a shock is driven upstream, producing the pileup seen as the emission loop. Because of its low shock velocity, high density, and proximity to the central star, the shock should be isothermal and the loop material in photoionization equilibrium with the central star. The thermal pressure in the loop should match the ram pressure of the stellar wind; that is, $P_w/k = 2.2 n_p T_p$, assuming helium is singly ionized as before ($n_e = 1.1 n_p$). With $T = 7950$ K from our spectra of the inner knots, $n_p = 4200$ cm^{-3}.

The density of the loop material can be estimated from its geometry and surface brightness. As shown in Paper II, at nebular temperatures the Hα emission measure is

$$\mathrm{EM} = 10^7 \times \mathrm{SB}(\mathrm{H}\alpha) 10^{C(\mathrm{H}\alpha)} T_4^{-1} \ \mathrm{cm}^{-6} \ \mathrm{pc}\,, \qquad (4)$$

where SB(Hα) is given in ergs cm^{-2} s^{-1} sr^{-1}. The density within a given portion of the loop can be calculated from its line-of-sight column depth, estimated via the geometry of the emitting region. With $C(\mathrm{H}\alpha) = 0.88$ derived from the STIS rim spectra, the density of the elliptical portion of the loop is 2500–3500 cm^{-3}. Given the large uncertainty inherent to the simplifying assumptions, we consider this result in reasonable agreement with the gas pressure result.

There is some countervailing evidence to the above scenario. The morphology of the knots and loop suggest that the most likely source of the flow is the brightest of the knots. The analysis above presumes an angle of projection of 35° relative to the plane of the sky; this should be true not only for the loop, but for the source of the flow as well.

However, in Paper II our estimate of the ionizing flux impinging on the brightest knot implies that the distance of the knot from the star is approximately equal to the projected distance; that is, a projection angle of 0°. It is unclear at this time how to reconcile these two results.

6. SUMMARY

NGC 7635 is the bubble formed by the interaction between the stellar wind of BD +60°2522 and its surroundings. Material from the surrounding H II region is swept up into a circular shell, with the central star well offset from its geometric center. This is likely the result of the distribution and motion of the material from which it is formed. The series of bright knots close to the star toward the west is revealed to be the ionized edge of a large mass of neutral material. The large stellar UV flux drives a strong photoevaporative flow from their surfaces, which diverts the shell material around them. The strongest of these flows may also be the source of material for an emission loop that appears between it and the star.

We have obtained the first direct measurement of T_e([O III]) for the bubble (8180 K), as well as the first C^{++}/H abundance for the nebula. Abundances are consistent with an H II region at the presumed Galactic distance except for a slight He enhancement in the rim, presumably from contamination by stellar wind material. There is a persistent factor of 2 difference in the oxygen abundance between the material in the rim and that in the inner knots. Line ratio and surface brightness maps from the high-resolution STIS spectra and the WFPC2 imagery show indications that the expansion of the bubble is only slightly supersonic, in agreement with previous radial velocity measurements.

The authors would like to thank Parviz Ghavamian for acquiring the Whipple spectra presented in this paper. This work was supported in part at all three institutions by AURA/STScI grant GO-7515. In addition, this work was supported at Arizona State University by NASA/JPL contracts 959289 and 959329 and Caltech contract PC 064528. B. D. M. acknowledges the support of AURA/STScI grant GO-08568.01-A to Rice University for postdoctoral support during the preparation of this paper. Work at South Carolina State was also supported by NASA/URC NCCW-0085, NASA/MU-SPIN NCC 5-534, NASA/OSS NAG 5-10145, and with a travel grant from the South Carolina Space Grant Consortium.

REFERENCES

Barlow, M. J., Cohen, M., & Gull, T. R. 1976, MNRAS, 176, 359
Christopoulou, P. E., Goudis, C. D., Meaburn, J., Dyson, J. E., & Clayton, C. A. 1995, A&A, 295, 509
Conti, P. S., & Alschuler, W. R. 1971, ApJ, 170, 325
Conti, P. S., Garmany, C. D., de Loore, C., & Vanbeveren, D. 1983, ApJ, 274, 302
Doroshenko, V. T. 1972, AZh, 49, 494 (English transl. Soviet Astron., 16, 402)
Dufour, R. J. 1989, Rev. Mexicana Astron. Astrofis., 18, 87
Esteban, C., Peimbert, M., Torres-Peimbert, S., & Escalante, V. 1998, MNRAS, 295, 401
Garmany, C. D., & Stencel, R. E. 1992, A&AS, 94, 211
Georgelin, Y. M. 1975, Ph.D. thesis, Univ. Provence
Høg, E., Kuzmin, A., Bastian, U., Fabricius, C., Kuimov, K., Lindegren, L., Makarov, V. V., & Röser, S. 1998, A&A, 335, L65
Holtzman, J. A., Burrows, C. J., Casertano, S., Hester, J. J., Trauger, J. T., Watson, A. M., & Worthey, G. 1995a, PASP, 107, 1065
Holtzman, J. A., et al. 1995b, PASP, 107, 156
Humphreys, R. M. 1978, ApJS, 38, 309
Icke, V. 1973, A&A, 26, 45
Israel, F. P., Habing, H. J., & de Jong, T. 1973, A&A, 27, 143
Johnson, H. M. 1974, A&A, 32, 17
Johnson, H. M. 1980, ApJ, 235, 66 (erratum 238, 1162)
———. 1982, ApJS, 50, 551
Leitherer, C. 1988, ApJ, 326, 356
Lynds, B. T., & O'Neil, E. J., Jr. 1983, ApJ, 274, 650
Moore, B. D., Hester, J. J., Scowen, P. A., & Walter, D. K. 2002, AJ, 124, 3305 (Paper II)
Sabbadin, F., & Bianchini, A. 1977, A&A, 55, 177
Schmidt, M. 1965, in Stars and Stellar Systems, Vol. 5, Galactic Structure, ed. A. Blaauw (Chicago: Univ. Chicago Press), 513
Seaton, M. 1979, MNRAS, 187, 73P
Shaver, P. A., McGee, R. X., Newton, L. M., Danks, A. C., & Pottasch, S. R. 1983, MNRAS, 204, 53
Shaw, R. A., & Dufour, R. J. 1995, PASP, 107, 896
Shore, S. 1992, An Introduction to Astrophysical Hydrodynamics (San Diego: Academic)
Smits, D. P. 1996, MNRAS, 278, 683
Talent, D. L., & Dufour, R. J. 1979, ApJ, 233, 888
Thronson, H. A., Jr., Lada, C. J., Harvey, P. M., & Werner, M. W. 1982, MNRAS, 201, 429
Trauger, J. T., et al. 1994, ApJ, 435, L3
Vacca, W. D., Garmany, C. D., & Shull, J. M. 1996, ApJ, 460, 914
Whitford, A. E. 1958, AJ, 63, 201